



Dual-beam manually-actuated distortion-corrected imaging (DMDI) with micromotor catheters

ANTHONY M. D. LEE,^{*} GEOFFREY HOHERT, PATRICIA T. ANGKIRIWANG, CALUM MACAULAY, AND PIERRE LANE

Imaging Unit – Department of Integrative Oncology, British Columbia Cancer Agency Cancer Research Centre, Vancouver, BC V5Z 1L3, CANADA

**alee@bccrc.ca*

Abstract: We present a new paradigm for performing two-dimensional scanning called dual-beam manually-actuated distortion-corrected imaging (DMDI). DMDI operates by imaging the same object with two spatially-separated beams that are being mechanically scanned rapidly in one dimension with slower manual actuation along a second dimension. Registration of common features between the two imaging channels allows remapping of the images to correct for distortions due to manual actuation. We demonstrate DMDI using a 4.7 mm OD rotationally scanning dual-beam micromotor catheter (DBMC). The DBMC requires a simple, one-time calibration of the beam paths by imaging a patterned phantom. DMDI allows for distortion correction of non-uniform axial speed and rotational motion of the DBMC. We show the utility of this technique by demonstrating *en face* OCT image distortion correction of a manually-scanned checkerboard phantom and fingerprint scan.

© 2017 Optical Society of America

OCIS codes: (110.0110) Imaging systems; (170.2150) Endoscopic imaging; (170.3890) Medical optics instrumentation; (120.5800) Scanners; (110.3010) Image reconstruction techniques.

References and links

1. D. C. Adams, Y. Wang, L. P. Hariri, and M. J. Suter, "Advances in endoscopic optical coherence tomography catheter designs," *IEEE J. Sel. Top. Quantum Electron.* **22**(3), 210–221 (2016).
2. J. G. F. Chao Zhou, T. H. Tsai, and H. Mashimo, "Endoscopic optical coherence tomography," in *Optical Coherence Tomography: Technology and Applications*, 2nd ed., W. D. a. J. G. Fujimoto, ed. (2015), pp. 2077–2108.
3. T. Adriaenssens and G. J. Ughi, "Recent advances in the field of optical coherence tomography," *Curr. Cardiovasc. Imaging Rep.* **10**(7), 23 (2017).
4. T.-H. Tsai, J. G. Fujimoto, and H. Mashimo, "Endoscopic optical coherence tomography for clinical gastroenterology," *Diagnostics (Basel)* **4**(2), 57–93 (2014).
5. M. J. Gora, M. J. Suter, G. J. Tearney, and X. Li, "Endoscopic optical coherence tomography: technologies and clinical applications [Invited]," *Biomed. Opt. Express* **8**(5), 2405–2444 (2017).
6. A. Ahmad, S. G. Adie, E. J. Chaney, U. Sharma, and S. A. Boppart, "Cross-correlation-based image acquisition technique for manually-scanned optical coherence tomography," *Opt. Express* **17**(10), 8125–8136 (2009).
7. X. Liu, Y. Huang, and J. U. Kang, "Distortion-free freehand-scanning OCT implemented with real-time scanning speed variance correction," *Opt. Express* **20**(15), 16567–16583 (2012).
8. Y. Wang, Y. Wang, A. Akansu, K. D. Belfield, B. Hubbi, and X. Liu, "Robust motion tracking based on adaptive speckle decorrelation analysis of OCT signal," *Biomed. Opt. Express* **6**(11), 4302–4316 (2015).
9. Y. Huang, X. Liu, C. Song, and J. U. Kang, "Motion-compensated hand-held common-path Fourier-domain optical coherence tomography probe for image-guided intervention," *Biomed. Opt. Express* **3**(12), 3105–3118 (2012).
10. N. Uribe-Patarroyo and B. E. Bouma, "Rotational distortion correction in endoscopic optical coherence tomography based on speckle decorrelation," *Opt. Lett.* **40**(23), 5518–5521 (2015).
11. B. Y. Yeo, R. A. McLaughlin, R. W. Kirk, and D. D. Sampson, "Enabling freehand lateral scanning of optical coherence tomography needle probes with a magnetic tracking system," *Biomed. Opt. Express* **3**(7), 1565–1578 (2012).
12. N. Iftimia, G. Maguluri, E. W. Chang, S. Chang, J. Magill, and W. Brugge, "Hand scanning optical coherence tomography imaging using encoder feedback," *Opt. Lett.* **39**(24), 6807–6810 (2014).
13. P. Pande, G. L. Monroy, R. M. Nolan, R. L. Shelton, and S. A. Boppart, "Sensor-based technique for manually scanned hand-held optical coherence tomography imaging," *J. Sens.* **2016**, 1–7 (2016).

14. B. Lau, R. A. McLaughlin, A. Curatolo, R. W. Kirk, D. K. Gerstmann, and D. D. Sampson, "Imaging true 3D endoscopic anatomy by incorporating magnetic tracking with optical coherence tomography: proof-of-principle for airways," *Opt. Express* **18**(26), 27173–27180 (2010).
15. J. C. Jing, L. Chou, E. Su, B. J. F. Wong, and Z. Chen, "Anatomically correct visualization of the human upper airway using a high-speed long range optical coherence tomography system with an integrated positioning sensor," *Sci. Rep.* **6**(1), 39443 (2016).
16. D. C. Adler, C. Zhou, T.-H. Tsai, J. Schmitt, Q. Huang, H. Mashimo, and J. G. Fujimoto, "Three-dimensional endomicroscopy of the human colon using optical coherence tomography," *Opt. Express* **17**(2), 784–796 (2009).
17. M. J. Gora, J. S. Sauk, R. W. Carruth, K. A. Gallagher, M. J. Suter, N. S. Nishioka, L. E. Kava, M. Rosenberg, B. E. Bouma, and G. J. Tearney, "Tethered capsule endomicroscopy enables less invasive imaging of gastrointestinal tract microstructure," *Nat. Med.* **19**(2), 238–240 (2013).
18. K. Liang, G. Traverso, H.-C. Lee, O. O. Ahsen, Z. Wang, B. Potsaid, M. Giacomelli, V. Jayaraman, R. Barman, A. Cable, H. Mashimo, R. Langer, and J. G. Fujimoto, "Ultrahigh speed en face OCT capsule for endoscopic imaging," *Biomed. Opt. Express* **6**(4), 1146–1163 (2015).
19. A. M. D. Lee, L. Cahill, K. Liu, C. MacAulay, C. Poh, and P. Lane, "Wide-field in vivo oral OCT imaging," *Biomed. Opt. Express* **6**(7), 2664–2674 (2015).
20. H. Pahlevaninezhad, A. M. D. Lee, T. Shaipanich, R. Raizada, L. Cahill, G. Hohert, V. X. D. Yang, S. Lam, C. MacAulay, and P. Lane, "A high-efficiency fiber-based imaging system for co-registered autofluorescence and optical coherence tomography," *Biomed. Opt. Express* **5**(9), 2978–2987 (2014).

1. Introduction

Two-dimensional scanning mechanisms, of which there are many demonstrated implementations [1, 2], are required for many endoscopic imaging modalities such as three-dimensional optical coherence tomography (OCT). Such scanners have been used to acquire 3D OCT images from many confined internal body sites including the coronary arteries, upper and lower gastrointestinal tracts, and respiratory tract [3–5]. Fiber optic rotary catheters that are either distally or proximally rotated are ideal for imaging long segments of tubular organs. Distally rotated catheters commonly employ stationary optical fibers directed toward an angled mirror that is spun by a micromotor, whereas in proximally rotated catheters, the entire optical fiber and beam-directing optics are rotated by an externally located motor. Each method has its advantages and disadvantages depending on the desired application.

Axial scanning along the second dimension is accomplished by pulling back the rotary catheter in a controlled fashion using a linear motor or by hand. Linear motor actuation generally produces evenly pitched, distortion-free imaging. However, patient or clinician motion artifacts can distort the images along the pullback axis. Additionally, the length of pullback is limited by the stroke of the linear actuator, necessitating multiple overlapping pullbacks for long imaging lengths.

Manual actuation along the pullback axis is attractive because it can greatly simplify the catheter construction and operation. This may result in cheaper, smaller, and more reliable catheters that will have greater clinical applicability. Additionally, the length of a manually-actuated pullback is only limited by the storage of the data acquisition system. However, the primary drawback of manual actuation is non-uniform pullback speed (NUPS) that can smear out or compress features along the pullback axis making image interpretation and analysis along this axis difficult.

A number of groups have investigated methods for correcting or tracking manually-scanned optical probes. Oversampling and correlation between A-scans have been used to correct for speed variation in 1-dimensional scanning for 2D optical coherence tomography (OCT) imaging [6–10]; however, due to the large mismatch in linear scanning speeds of rotary and pullback motion, extension of these methods to 2D rotary-pullback scanning is not straightforward. Magnetic sensors, and optical motion tracking encoders or sensors have also been used to discern scan motion in handheld OCT systems, although miniaturization into endoscopic catheters has yet to be realized [11–13]. Groups have demonstrated 3-dimensional anatomical imaging by reconstructing the pathway taken by OCT catheters with integrated electromagnetic tracking sensors but these efforts require a considerably greater degree of instrumental complexity [14, 15].

In this work, we present a new 2D scanning paradigm called Dual-beam Manually-actuated Distortion-corrected Imaging (DMDI). Conceptually, DMDI requires two imaging beams that scan mechanically along one dimension (fast axis) and are separated by a known distance in the orthogonal dimension (slow axis). As the sample is manually scanned primarily along the slow axis direction, measurement of the time difference between when the second beam passes by a feature also seen by the first beam can allow determination of the average scan speed and direction between those times. Knowledge of the scan speed and direction allows re-mapping of the distorted images from either of the beams to produce the distortion-corrected image.

We demonstrate an example of DMDI in a rotationally scanning dual-beam micromotor catheter (DBMC). The micromotor scans the fast axis in a rotational manner while motion along the axial axis is manually actuated. We first describe the calibration procedure of the DBMC to determine the scan paths of the beams. We then demonstrate the distortion correction procedure by imaging a patterned phantom. Finally, we show *in vivo* DMDI of a fingerprint pattern.

2. Methods

2.1 OCT imaging system

For the convenience of equipment in our lab, we use *en face* OCT as the imaging modality for this demonstration of DMDI, although in principle, any point-scanning imaging modality could be used. The employed dual-channel imaging OCT system is schematically shown in Fig. 1(i). A 23 mW, 100 kHz 1310 nm swept-source laser (AXP50125-6, Axsun Technologies, Billerica, MA) is 50/50 split and fed into two parallel Mach-Zehnder OCT interferometers. The sample arms of each of these interferometers feeds into one of the fiber pigtails of the DBMC. OCT signals from balanced detectors (PDB480C-AC, Thorlabs, Inc.) from each of the interferometers are simultaneously acquired by a dual-channel, k-clocked fast digitizer (ATS9350, Alazar Technologies, Inc., Pointe Claire, QC). The path length difference between the two interferometers is approximately 2 m, sufficiently different such that there is no OCT cross-talk between them.

2.2 Dual beam micromotor catheter (DBMC)

The dual beam micromotor catheter (DBMC) used for these experiments is shown in Fig. 1(ii-iv). A dual SMF-28 fiber pigtail (DFP, KFP-V-2-8D-250S-250-1310-FC/APC, Photop Technologies, Inc., Santa Clara, CA) was aligned to a GRIN lens (GRIN2313A, Thorlabs Inc., Newton, NJ) using a glass ferrule (51-2800-1800, Thorlabs, Inc.). Both the DFP and GRIN lens were polished at 8° and anti-reflection coated for 1310 nm. The fibers within the DFP are separated by 250 μm and oriented vertically to one another if viewing the 8° polish angle from the side. The distance between the DFP and GRIN was adjusted to place the focus of a 1310 nm light source approximately 3.5 mm from the end face of the GRIN with a circular spot size of 14 μm measured with a beam profiler (BeamMap2, DataRay Inc., Redding, CA). An aluminum-coated 1 mm right angle prism (MPCH-1.0, Tower Optical Corporation, Boynton Beach, FL) was mounted to the shaft of a 4 mm OD micromotor (SBL04-0829, Namiki Precision of California, Inc., Belmont, CA) with a bead of UV-curing adhesive (NOA 63, Norland Products Inc., Cranbury, NJ) at approximately 8° angle to avoid strong back-reflections within the system. The DFP assembly was inserted into a plastic tube with the same outer diameter as that of the micromotor. The flexible printed circuit (FPC) feeding power to the micromotor was bent back alongside the motor and held against it with another section of thin-walled plastic tube giving an overall catheter OD of 4.7 mm. The minimum rigid length of the catheter is 28 mm. The imaging power at the sample was 2.1 and 2.4 mW for the A and B beams respectively. A commercial driver board (SOD12ST, Namiki Precision of California, Inc.) was used to drive the micromotor at 100 Hz for all experiments

described in this paper. No frame-to-frame non-uniform rotational distortion (NURD) was observed when using this motor and driver combination.

The light paths for the two imaging beams are approximately shown in Fig. 1(ii-iii). Due to the 8° polish on the DFP exit face, one beam (beam A, red line) deflects and enters the GRIN near on-axis, hits the prism near center, and traces a roughly planar circular pattern on the catheter outer diameter. The other beam (beam B, blue line) deflects away from the GRIN axis, hits the prism off-center, and traces a non-planar elliptical pattern on the catheter outer diameter.

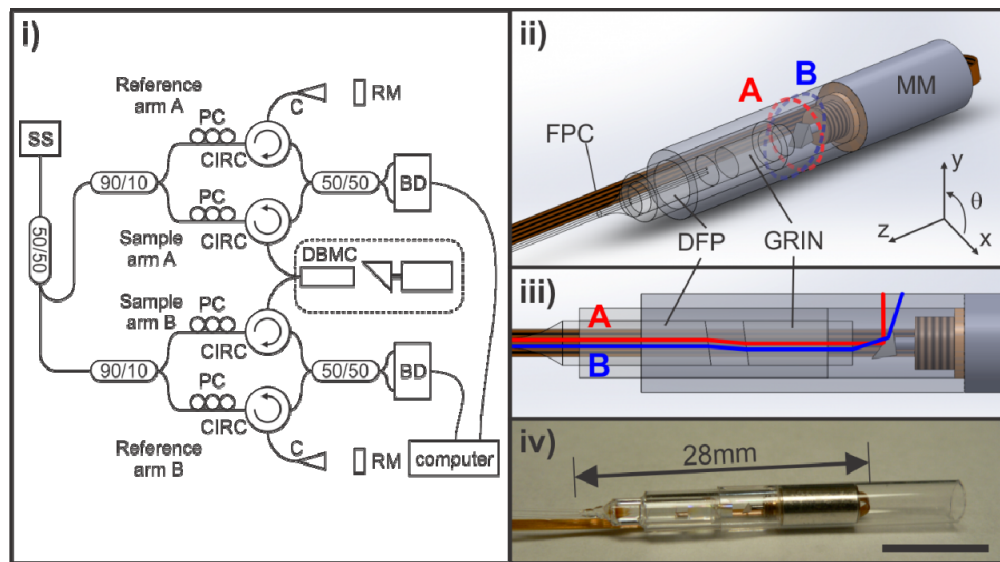


Fig. 1. Dual-channel OCT imaging system and dual beam micromotor catheter (DBMC). i) Schematic diagram of dual-channel OCT imaging system. SS = swept-source laser, PC = polarization controller, C = collimator, RM = reference mirror, CIRC = circulator, BD = balanced detector. ii) Model of DBMC (outermost plastic tubing not shown). DFP = dual fiber pigtail; GRIN = graded-index lens; MM = 4 mm OD micromotor, FPC = flexible printed circuit. Approximate paths of A and B beams at catheter outer diameter are shown in red and blue respectively. iii) Side view of DBMC showing approximate beam paths for A and B beams. iv) Photograph of the DBMC. The rigid length of the DBMC is indicated. Scale bar is 1 cm.

2.3 DBMC calibration

For calibration of the DBMC, a pattern consisting of groups of equally spaced, horizontal and vertical black lines was printed on standard white printer paper. This pattern was rolled around and taped over a 4.75/5.00 mm ID/OD plastic tube that slides easily but snugly over the DBMC. Care was taken during rolling to ensure that the circumferential lines were continuous at the paper seam. Imaging of the calibration pattern involved first stationary imaging of the lines parallel to the plastic tube axis. Following this, a linear stepper motor pushed the DBMC through the circumferential line pattern at a constant speed of 4 mm/s.

The major steps for calibrating the DBMC are outlined in the left panel of Fig. 2 and are described in more detail here. For calibration, after a small delay at the start of the data acquisition, the DBMC was pushed through the calibration phantom at $v_z = 4\text{mm/s}$. The two imaging channels, A and B, are acquired as continuous streams of equally time-spaced A-lines with index N . Figure 3(i) shows *en face* OCT images $A(n, fr)$ and $B(n, fr)$, where the frame index, fr , is the integer division of N by N_{fr} , the number of A-lines per frame ($N_{fr} = 100,000$ A-lines per second / 100 frames per second), and n is the remainder. The *en face* OCT images are presented as mean intensity projections over the OCT depth dimension because the printed paper phantom has no encoded depth information. Each fr column of the

image represents one rotation of the DBMC mirror, while n represents an angular position of the prism. Although N , fr and n are functions of time t and should be written as $N(t)$, $fr(t)$, and $n(t)$, for notational simplicity the time dependence is not explicitly stated in further discussion. Apparent in the displayed images as a set of darker horizontal lines is the FPC at the top of image A and straddling the top/bottom border of image B that occludes imaging. The shift of the FPC position (and the rest of the pattern in general) between the two channels is indicative that the A and B channels image each point on the DBMC outer diameter at different fr and n values, therefore, at different times.

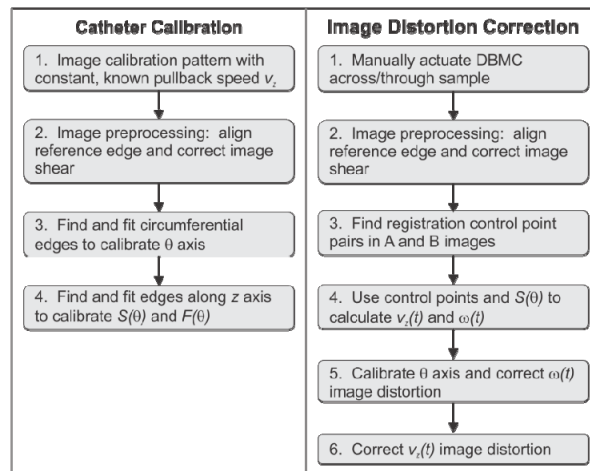


Fig. 2. Outline of primary DMDI processing steps for (left) calibration and (right) distortion correcting images acquired with DBMCs.

The FPC is stationary relative to the A and B imaging positions throughout the scan so the small downwards drift (see small increasing gap towards top right of the A image) of the FPC in Fig. 3(i) from left to right is due to the asynchronous operation of the micromotor and the laser-triggered OCT data acquisition system. This small amount of image shear can be corrected by interpolating the continuous stream of A-lines so that the image frames are aligned. After shear-correction, the horizontal lines of the calibration phantom during the pushed portion of imaging still appear tilted due to a small amount of catheter rotation during axial actuation. Choosing $N_{ref,(A,B)}$ as the index of the A-line corresponding to the bottom edge of the FPC in both images, the images can be aligned by plotting as $A(n_A, fr_A)$ and $B(n_B, fr_B)$, where $fr_{(A,B)}$ is the integer division of $N - N_{ref,(A,B)}$ by N_{fr} and $n_{(A,B)}$ is the remainder. (Note: Here we use the subscripted (A,B) to represent two distinct terms or functions corresponding to each of the A and B imaging channels).

The equally-spaced horizontal lines of the printed phantom are approximately equally spaced in image A because the A beam hits near-center on the spinning prism and it scans the catheter outer diameter at roughly constant speed. However, the horizontal lines in image B are expanded at the top and compressed at the bottom because the B beam hits the spinning prism away from the rotational axis and thus scans the catheter outer diameter on one side of the catheter faster than the opposite side. Therefore, the first step in DBMC calibration is to find how index N maps to $\theta_{(A,B)}$, the angular positions for each beam at the catheter surface.

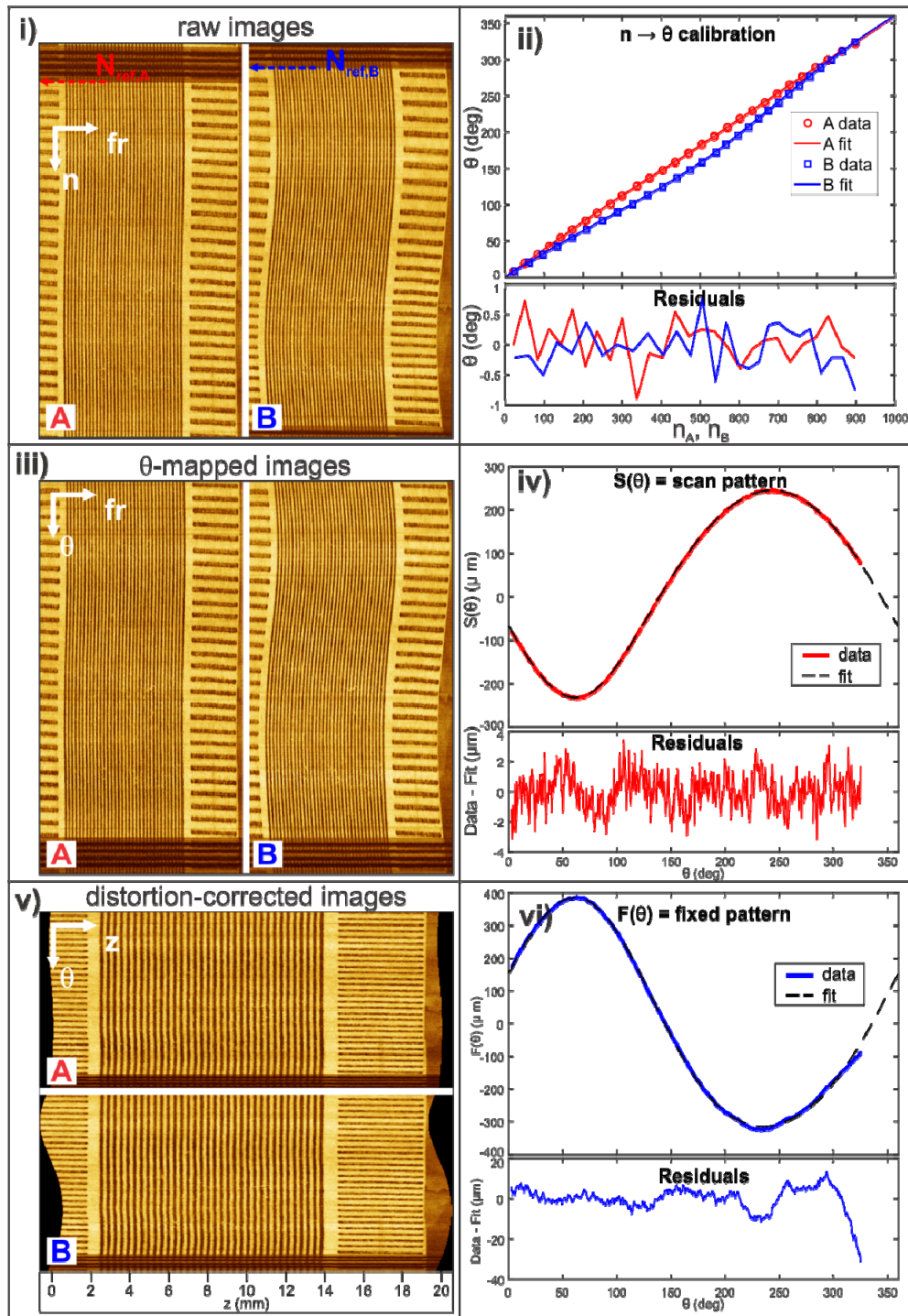


Fig. 3. Calibration of DBMC using the paper calibration pattern. i) Raw *en face* OCT images from A and B channels. The range of the n axis is from 1 to 1000 A-lines, with each image column corresponding to one rotation of the prism. ii) Data and fit of positions of horizontal lines in i). iii) Aligned, shear-corrected, and θ calibrated images. The range of the θ axis is from 0° to 360° . iv) Scan pattern data and fit. v) Distortion corrected images. vi) Fixed pattern data and fit.

The $\theta_{(A,B)}(n_{(A,B)})$ calibrations were performed by averaging over the first 6 stationary (non-pushed) frames and thresholding the images to determine the positions $n_{(A,B)j}$ of the negative-going edges of the horizontal lines in images A and B. Only the negative-going edges were used for calibration as the phantom printing process does not ensure that the heights of the light and dark horizontal bars in the images are equal. The equally-spaced negative-going edges at angular positions θ_j , where j represents the j^{th} edge position, correspond to $n_{A,j}$ and $n_{B,j}$ in images A and B respectively. θ_j can be represented as

$$\theta = \theta_0 + j(\Delta\theta) \quad (1)$$

where θ_0 is the offset from the bottom edge of the FPC (in the same direction as increasing n) to the first negative-going edge; and $\Delta\theta$ is the spacing of the negative-going edges, both of these are in units of degrees. The calibration from $n_{(A,B)}$ to $\theta_{(A,B)}$ can be expressed as a linear term plus a k^{th} -order cosine expansion with amplitudes and offsets $c_{(A,B),k}$ and $n_{(A,B),k,off}$ respectively, and periodic in N_{fr} :

$$\theta_{(A,B)}(n_{(A,B)}) = g \cdot n_{(A,B)} + g \sum_k c_{(A,B),k} \cos\left(\frac{2\pi k}{N_{fr}}(n_{(A,B)} - n_{(A,B),k,off})\right) - g \cdot C_{(A,B),0} \quad (2)$$

where $g = \frac{360^\circ}{1000 \text{ A-lines}}$. The terms $C_{(A,B),0}$ ensure that $\theta_{(A,B)}(n_{(A,B)} = 0) = 0$, and are

$$C_{(A,B),0} = g \sum_k c_{(A,B),k} \cos\left(\frac{2\pi k}{N_{fr}}(-n_{(A,B),k,off})\right) \quad (3)$$

Using Eqs. (1)-(3), the sets of $[\theta_j, n_{A,j}]$ and $[\theta_j, n_{B,j}]$ pairs were used to empirically fit for the unknown parameters θ_0 , $\Delta\theta$, $c_{(A,B),k}$ and $n_{(A,B),k,off}$. Least-squares minimization was used to find optimized set of parameters for Eqs. (1)-(3) with truncation of the cosine expansion at increasing values of k . The second-order truncation with the parameters shown in Table 1 was found to be sufficient to reduce the residuals between the fit and data to statistical noise variation. The plots of the data, second-order fits, and residuals of Eq. (2) for the DBMC used in this work are shown in Fig. 3(ii). Using the fitted parameters, the $A(n_{A,j}fr_A)$ and $B(n_{B,j}fr_B)$ images can be re-mapped to $A(\theta, fr_A)$ and $B(\theta, fr_B)$, as shown in Fig. 3(iii).

Table 1. Fit parameters for θ calibration

Parameter	Value	Parameter	Value
θ_0	7.8°		
$\Delta\theta$	11.7°		
c_{A1}	-4.46 A-lines	c_{B1}	32.7 A-lines
$N_{A1,off}$	-189.1 A-lines	$N_{B1,off}$	-26.6 A-lines
c_{A2}	3.50 A-lines	c_{B2}	3.2 A-lines
$N_{A2,off}$	-256.8 A-lines	$N_{B2,off}$	-200.0 A-lines

The next step in the DBMC calibration makes use of the constant-speed actuated part of the images across the vertical lines of the calibration pattern to determine the scanning pattern of the imaging beams. The θ -calibrated images were smoothed with a Gaussian kernel and then a threshold was applied to obtain a binary mask. The frame indices of the edges of the vertical lines were identified for each image θ -row. As the vertical lines are equally spaced in the calibration pattern along z , the frame indices for each θ -pixel can be analyzed using simple linear regression of the frame index versus edge number yielding slopes $m_{(A,B)}(\theta)$ in units of frames per edge, and intercepts $b_{(A,B)}(\theta)$ in units of frames. The slopes for both A and B channels should be identical for all values of θ , such that $m_A(\theta) = m_B(\theta) = m$. The intercepts $b_{(A,B)}(\theta)$ describe the average shape of the vertical lines as a function of θ in each of the A and B images in units of frames. For accuracy, the intercepts were fitted relative to the centermost

vertical line of the calibration pattern. We define the functions $S_{fr}(\theta)$ and $F_{fr}(\theta)$, the scan pattern and fixed pattern in units of frames, respectively, as

$$S_{fr}(\theta) = \frac{1}{2} [b_A(\theta) - b_B(\theta)] \quad (4)$$

$$F_{fr}(\theta) = \frac{1}{2} [b_A(\theta) + b_B(\theta)] \quad (5)$$

The scan and fixed pattern functions in units of distance, $S(\theta)$ and $F(\theta)$, can be calculated using

$$S(\theta) = [S_{fr}(\theta) \cdot N_{fr} + n_A(\theta) + N_{ref,A} - n_B(\theta) - N_{ref,B}] \cdot \frac{v_z}{f_{laser}} \quad (6)$$

$$F(\theta) = [F_{fr}(\theta) \cdot N_{fr} + n_A(\theta) + N_{ref,A} - n_B(\theta) - N_{ref,B}] \cdot \frac{v_z}{f_{laser}} \quad (7)$$

where $n_A(\theta)$ and $n_B(\theta)$ are found by solving the inverse of Eq. (2), f_{laser} is the laser sweep rate, and v_z is the specified axial speed. $S(\theta)$ and $F(\theta)$ for the DBMC used in this work are plotted as solid lines in Figs. 3(iv) and 3(vi) respectively. The scan pattern function $S(\theta)$ describes the distance between the A and B light beams as a function of θ , which is needed for calculation of the axial speed for DMDI. The fixed pattern function $F(\theta)$ describes the deviation from a perfect circle of the midpoint between the A and B light beams. Again being periodic in N_{fr} , $S(\theta)$ and $F(\theta)$ can be fit to sine expansions:

$$S(\theta) = s_0 + \sum_k s_k \sin\left(\frac{2\pi k}{N_{fr}}(\theta - \theta_{s,k,off})\right) \quad (8)$$

$$F(\theta) = f_0 + \sum_k f_k \sin\left(\frac{2\pi k}{N_{fr}}(\theta - \theta_{f,k,off})\right) \quad (9)$$

$S(\theta)$ and $F(\theta)$ were empirically fit via least squares minimization with the fitted parameters shown in Table 2. The fits of $S(\theta)$ and $F(\theta)$ are shown as dashed lines in Figs. 3(iv) and 3(vi) respectively, along with their corresponding residuals below. $S(\theta)$ was truncated at 3rd-order after reducing the 4th-order residuals to the approximate noise level while $F(\theta)$ was truncated at 2nd-order as further expansion did not improve the fit substantially. The larger residuals between $\theta = 300^\circ$ and 330° for $F(\theta)$ are likely due to the presence of the underlying FPC that causes non-circular deformation at the outer diameter at these angles; in addition, the printed paper pattern overlaps itself near these angles, which causes the paper to be further from the outer diameter of the plastic tube.

Table 2. Fit parameters for $S(\theta)$ and $F(\theta)$ calibrations

Parameter	Value	Parameter	Value
s_0	27.7 μm	f_0	8131.1 μm
s_1	-235.1 μm	f_1	349.4 μm
$\theta_{s1,off}$	-27.8 $^\circ$	$\theta_{f1,off}$	-30.4 $^\circ$
s_2	-22.0 μm	f_2	35.8 μm
$\theta_{s2,off}$	-14.1 $^\circ$	$\theta_{f2,off}$	21.3 $^\circ$
s_3	3.5 μm		
$\theta_{s3,off}$	-28.7 $^\circ$		

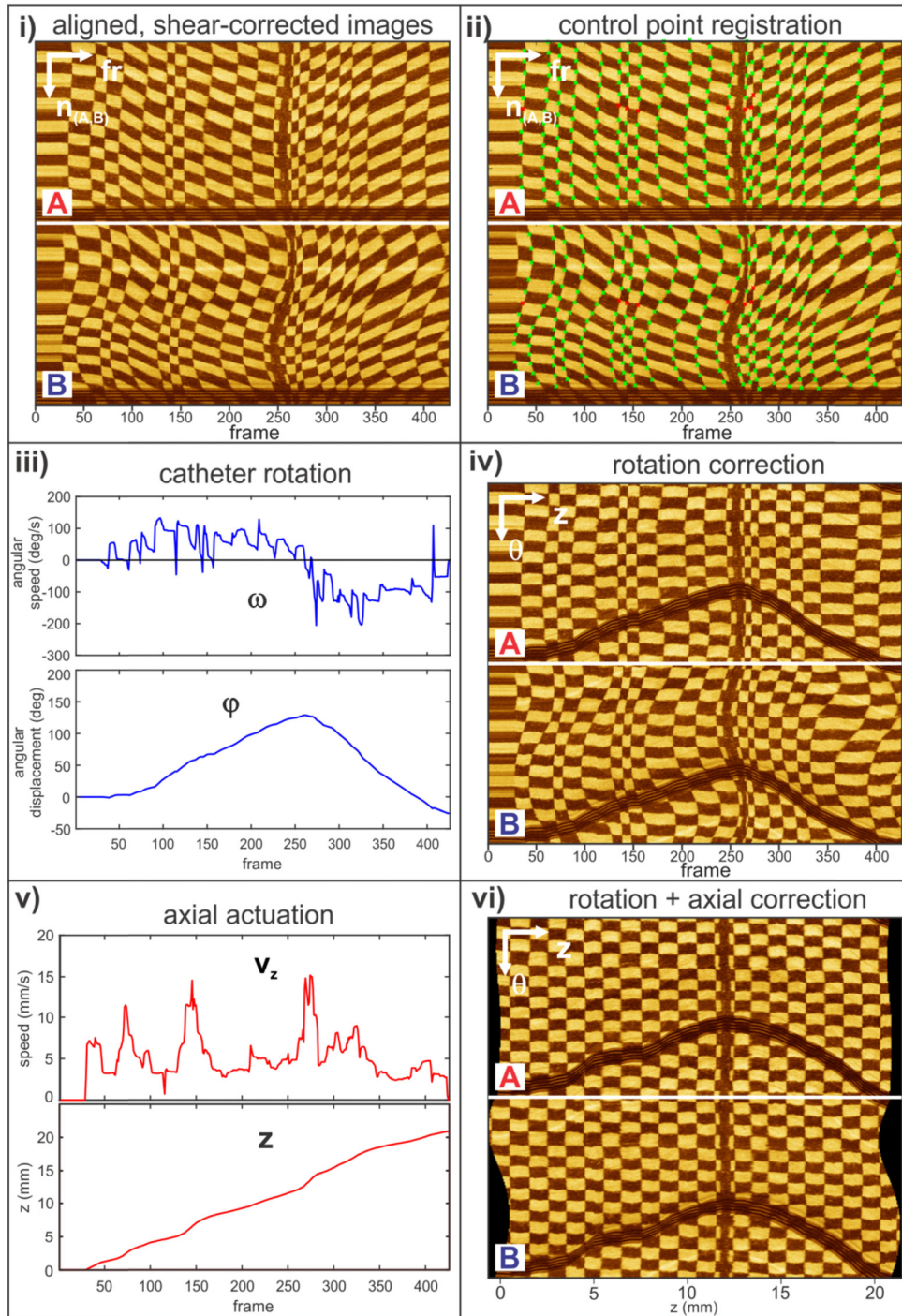


Fig. 4. Image correction of 1mm checkerboard pattern with manual axial and rotational actuation. i) Aligned and shear-corrected images of channels A and B. ii) Control points ($n = 303$) used for A/B image registration. Green points ($n = 295$) were used for distortion correction, while red points ($n = 8$) were omitted. iii) Catheter rotation characterization. iv) Axial actuation characterization. v) Rotation distortion-corrected images. vi) Rotation and axial distortion-corrected images.

To generate the distortion corrected images, the images must be adjusted to account for the overall motion of the DBMC and also for the apparent distortions due to the scan and fixed patterns. The z position of any point in the A and B images is given by

$$z_A(\theta, t) = z_{DBMC}(t) - S(\theta) - F(\theta) \quad (10)$$

$$z_B(\theta, t) = z_{DBMC}(t) + S(\theta) - F(\theta) \quad (11)$$

where $z_{DBMC}(t) = \int v_z(t') dt'$ is the axial position of the DBMC. As $F(\theta)$ is subtracted in both Eqs. (10) and (11), the constant offset term f_0 in Eq. (9) can be ignored. Using the constant axial velocity of 4 mm/s and Eqs. (10) and (11), $A(\theta, fr_A)$ and $B(\theta, fr_B)$ can be remapped to the distortion corrected images $A(\theta, z)$ and $B(\theta, z)$, as shown in Fig. 3(v).

2.4 Image distortion correction

A phantom to test the developed distortion correction algorithm was made by printing a 1 mm checkerboard pattern on paper and wrapping around a 4.75/5.00 mm ID/OD plastic tube (same as was used for the calibration pattern). An extra registration line was printed within the pattern to allow definite identification and correlation of each of the checkerboard squares in both of the images. After the start of acquisition, the DBMC was manually pushed through the test phantom at varying speed while also rotating it about the catheter axis. The overall acquisition time was a few seconds.

Once the calibration functions $S(\theta)$ and $F(\theta)$ for a DBMC are known, it can be used to produce distortion-corrected images using the process outlined on the right side of Fig. 2. $A(n_A, fr_A)$ and $B(n_B, fr_B)$ images of the 1 mm checkerboard pattern imaged with the DBMC after reference edge alignment and shear correction are shown in Fig. 4(i). The non-constant axial velocity and angular rotation of the DBMC during actuation are readily apparent. Starting from the dark vertical line approximately in the centre of the image, all vertices common to both A and B were manually registered using the MATLAB (Mathworks, Inc., Natick, MA) `cpslect` function as $[(n_A, fr_A), (n_B, fr_B)]_j$ ($j = 1 \dots 303$) coordinate pairs. The registered control points are shown as green and red x's in Fig. 4(ii). The average z velocity $\bar{v}_{z,AB,j}$, between the j^{th} pair of registered control points can be estimated as

$$\bar{v}_{z,AB,j} = \frac{S(\theta_{A,j}) + S(\theta_{B,j})}{|t_{A,j} - t_{B,j}|} \quad (12)$$

where the numerator and denominator are the distance and time differences between the control points respectively, and $t_{(AB),j} = n_{(AB),j} / f_{laser}$. Similarly, the average angular velocity $\bar{\omega}_{AB,j}$ between the j^{th} pair of registered control points can be estimated as

$$\bar{\omega}_{AB,j} = \frac{\theta_{second,j} - \theta_{first,j}}{|t_{A,j} - t_{B,j}|} \quad (13)$$

where $\theta_{first,j}$ and $\theta_{second,j}$ are the θ values for the control points that are first and second in time respectively. Control point pairs with identical values of fr_A and fr_B were eliminated from further analysis because the errors associated with the manual selection of these control points are relatively large compared to the time differences being measured. The eliminated control points ($n = 8$) are shown as red x's in Fig. 4(ii), while all others are shown in green ($n = 295$). To estimate the instantaneous z and angular velocity at all values of time, vectors $v_z(t)$ and $\omega(t)$ were created where the individual elements are an equally weighted average of all $\bar{v}_{z,AB,j}$ and $\bar{\omega}_{AB,j}$, respectively, defined for that t . The axial speed at the beginning and ends of the

images where only a single beam imaged was set to an insignificantly small value – to have a single-valued $z_{(A,B)}(\theta, t)$ – and the axial speed was interpolated for times in the middle of the data set where axial speed was otherwise undefined. Plots of $\omega(t)$ and $v_z(t)$ averaged over each frame are shown in the upper panes of Figs. 4(iii) and 4(v) respectively. Integrating $\omega(t)$ and $v_z(t)$ over time gives the catheter angular displacement $\phi(t)$ and the catheter displacement $z_{DBMC}(t)$ as functions of time, respectively, shown averaged over each frame in the lower panes of Figs. 4(iii) and 4(v).

Performing the θ calibration step using Eqs. (2) and (3), and the fitted parameters in Table 1 gives the $A(\theta, fr_A)$ and $B(\theta, fr_B)$ images (not shown). To remove the image distortion caused by rotation of the DBMC, $\theta(t)$ needs to be remapped to $\theta'(t) = \theta(t) - \phi(t)$ to give the $A(\theta', fr_A)$ and $B(\theta', fr_B)$ images shown in Fig. 4(iv). Mapping of the z axis using Eqs. (10) and (11) produces images $A(\theta', z)$ and $B(\theta', z)$ shown in Fig. 4(vi).

3. Results

In vivo DMDI imaging was evaluated by fingerprint imaging. A 4.75/5.00 mm ID/OD plastic tube was grasped by three fingers while manually pushing the DBMC through it. The distortion correction procedure described in the proceeding section was performed on the manually-actuated finger imaging with the corresponding images shown in Fig. 5. Apart from the FPC, the dark horizontal bands in Fig. 5(i) correspond to the three spaces between the three fingers being scanned. Sweat ducts as indicated in Fig. 5(ii) were used as the registration control points. The full distortion-corrected images are shown in Fig. 5(iv).

4. Discussion

As can be seen in the imaging of the checkerboard pattern in Fig. 4, the 2D distortion correction procedure outlined in this work restores the original pattern quite well over a range of axial and rotational velocities. In the corrected images, the vertical lines of the pattern are straight and roughly 1 mm spaced, as designed. The horizontal lines are straight, though they have a downward tendency dropping approximately 17° over 20 mm length. This may be reflective of a small angle calibration error. For the finger imaging (Fig. 5), it is qualitatively easy to see that axial distortions are improved in the corrected images relative to the original image.

In DMDI, the maximum measurable axial velocity $v_{z,max}$, is the maximum distance separation of the two (or multiple) imaging beams S_{max} , multiplied by the frame rate of the fast axis f_{fr} :

$$v_{z,max} = S_{max} \cdot f_{fr} \quad (14)$$

For the DBMC used in this work $S_{max} = 0.48$ mm and $f_{fr} = 100$ Hz giving a maximum theoretical axial speed limit of 48 mm/s. Realistically, however, the maximum measurement speed is reduced by the uncertainty in selecting the registration control points, and by the fact that there may be no control points located near S_{max} . It is possible to increase $v_{z,max}$ by increasing S_{max} but this also increases the ‘dead’ (uncorrectable) zones at the beginning and ends of the scans where only one beam has scanned. Increasing f_{fr} can also increase $v_{z,max}$ as the micromotor used in this DBMC can spin much faster (>500 Hz) with a concomitant reduction in resolution along the fast axis.

For DBMCs, catheter rotation is in the same direction as the fast axis. As actuation of the DBMC is primarily along the axial axis, the maximum angular velocity that can be measured is far beyond what can be realized practically. The lower limit of angular velocity that can be measured is determined by the accuracy of the $\theta(N)$ calibration, the accuracy of shear correction, and the accuracy of selecting the registration control points.

While distortion correction using DMDI described here has only been applied to 2D *en face* OCT images, representative 3D OCT volumes could be generated by applying the same distortion correction to the corresponding dimensions of the original 3D OCT volumes.

However, these volumes would not necessarily be correct physical representations because the two imaging beams do not exit the catheter at the same angles. An improved distortion-correction algorithm that uses the full 3D OCT information should be possible that generates the physically-correct 3D OCT volume.

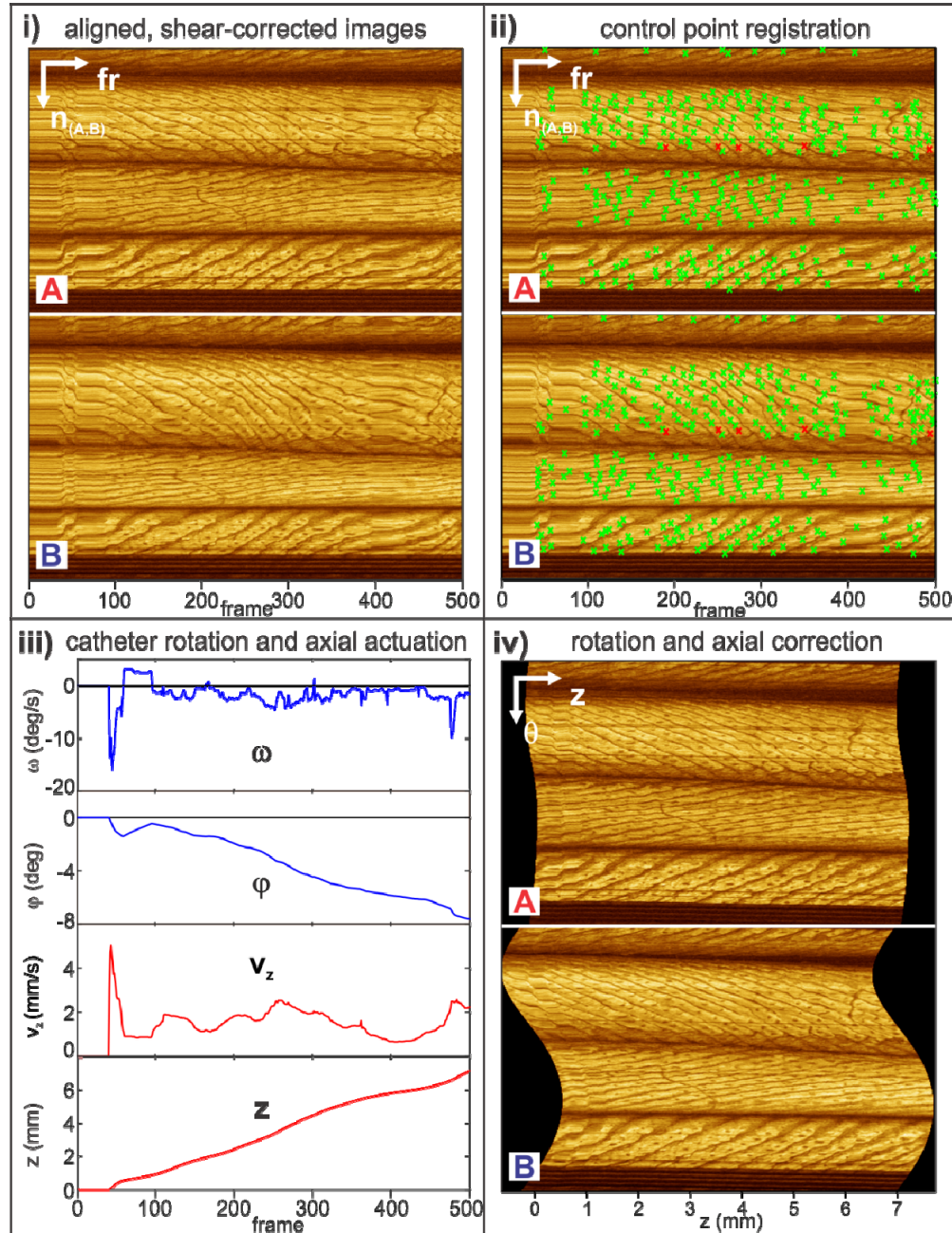


Fig. 5. Distortion correction for manually-actuated DBMC imaging across fingers. i) Aligned and shear-corrected images of channels A and B. ii) control points ($n = 312$) used for image registration. Green points ($n = 308$) were used for catheter angular and axial speed characterization, while red points ($n = 4$) were omitted. iii) Catheter angular rotation and axial displacement characterization. iv) Distortion-corrected images.

The biggest limitation in the implementation of DMDI described here is the laborious procedure of manually picking the numerous co-registered control points. Our group is currently working to automate this step to improve usability. Another potential problem arises if the images do not have enough sufficient unique features for co-registration, or conversely, if too many similar features frustrate unequivocal co-registration. These problems may be alleviated in OCT by using the depth dimension to increase or decrease the number of identifiable image features accordingly.

For DMDI with a DBMC, the need for only one mechanical scanner greatly simplifies the complexity of the catheter and driving mechanism, and perhaps expands capabilities for biomedical imaging applications. While correcting for distortions due to manual actuation, DMDI simultaneously corrects for axial and azimuthal motion artifacts due to voluntary or non-voluntary (cardiac, respiratory) patient motion as well as clinician motion. These motion artifacts are not easily corrected with single-channel rotary-pullback imaging catheters. Additionally, as the axial imaging length is not limited, a rotationally-scanning DBMC may be useful for distortion-corrected imaging in long cylindrically symmetric organs.

Using a DBMC, detailed OCT imaging of the entire colon, as was previously demonstrated with multiple image acquisitions [16], could potentially be acquired in a single data acquisition. A DBMC could also be implemented in a capsule-type device for esophageal OCT imaging, similar to those previously demonstrated [17, 18], but with reduced imaging distortions along the axial pullback axis. DBMCs based on smaller, commercially-available micromotors down to 0.9 mm OD could allow imaging of coronary arteries or other confined body sites. The current sized or a larger diameter DBMC could allow large field-of-view imaging of larger planar surfaces such as the oral cavity or skin, compared to previous demonstrations with rotary-pullback catheters [19]. Testing of DBMC imaging in these and other organ sites will be necessary to assess whether there are appropriate numbers of registration points to allow accurate DMDI distortion correction.

Endoscopic rotational 2D scanners are usually operated in a pullback fashion by first advancing the catheter past the region of interest (ROI) and then having controlled actuation back over the ROI. This is because the catheters must be advanced by hand slowly, and often with many pauses, to avoid tissue damage. Due to their speed-correcting ability, DBMCs can provide distortion-corrected imaging both in the push-forward and pullback directions. Imaging in the push-forward direction may allow better guidance of catheters, while also reducing the chances that valuable imaging sites are missed.

In this demonstration of DMDI, both imaging channels employed OCT imaging, resulting in redundant distortion-corrected images. However, the imaging modalities need not necessarily be identical, they are only required to have common identifiable features. For example, one channel could be single-mode fiber (SMF) to acquire OCT, and the other could be dual-clad fiber (DCF) to acquire OCT-autofluorescence imaging (OCT-AFI) [20]. It is known that the OCT channel in OCT-AFI provides inferior imaging compared to OCT imaging with SMF due to cross-coupling of the IR light between the inner cladding and core in DCF. However, the DCF OCT image quality should be sufficient to provide the image registration required to correct distortions in the SMF-acquired OCT image. In this way, both high quality OCT and AFI images could be obtained with a dual-modality DMDI device.

Although OCT was used in this demonstration of DMDI, any point imaging modality such as fluorescence or reflectance imaging could be used as well. Thus, this method is more widely applicable over methods that rely on speckle correlation/decorrelation.

5. Conclusion

To the best of our knowledge, this is the first demonstration using two beams and a fast one-dimensional scanner to produce two-dimensional manually-actuated, distortion-corrected images. We demonstrated the utility of this technique by constructing and calibrating a dual-

beam catheter that scans with a micromotor. We think that this technique will find many applications in biomedical optical imaging.

Funding

Canadian Institutes of Health Research (CIHR) and the National Science and Engineering Research Council of Canada (NSERC); BC Cancer Foundation Research Studentship Award.